High-resolution cross section measurements for neutron interactions on 89Y with incident neutron energies up to 95 keV

Eur. Phys. J. A manuscript No.
(will be inserted by the editor)

High-resolution cross measurements for neutron interactions with ^{89}Y for incident neutron energies up to 95 keV

G. Tagliente[1], P.M. Milazzo[2], C. Paradela[3], S. Kopecky[3], D. Vescovi[19,24], G. Alaerts[3], L.A. Damone[1,4], J. Heyse[3], M. Krtička[5], P. Schillebeeckx[3], A. Mengoni[6,7], R. Wynants[3], S. Valenta[5], O. Aberle[4], V. Alcayne[8], S.Amaducci[9,10], J. Andrzejewski[11], L. Audouin[12], V. Babiano-Suarez[13], M. Bacak[4,14,15], M. Barbagallo[4,1], V. Bécares[8], F. Bečvář[5], G. Bellia[9,10], E. Berthoumieux[15], J. Billowes[16], D. Bosnar[17], A.S. Brown[18], M. Busso[19,20], M. Caamaño[21], L. Caballero[22], M. Calviani[4], F. Calviño[22], D. Cano-Ott[8], A. Casanovas[22], F. Cerutti[4], Y.H. Chen[12], E. Chiaveri[16,23,4], N. Colonna[1], G.P. Cortés[22], M.A. Cortés-Giraldo[23], L. Cosentino[9], S. Cristallo[19,24], M. Diakaki[25], M. Dietz[26], C. Domingo-Pardo[13], R. Dressler[27], E. Dupont[15], I. Durán[21], Z. Eleme[28], B. Fernández-Domíngez[21], A.Ferrari[4], I. Ferro-Gonçalves[29], P. Finocchiaro[9], V. Furman[30], R. Garg[26], A. Gawlik[11], S. Gilardoni[4], T. Glodariu[31], K. Göbel[32], E. González-Romero[8], C. Guerrero[23], F. Gunsing[15], S. Heinitz[26], D.G. Jenkins[16], E. Jericha[14], Y. Kadi[4], F. Käppeler[33], A. Kimura[34], N. Kivel[27], M. Kokkoris[25], Y. Kopatch[30], D. Kurtulgil[32], I. Ladarescu[13], A.C. Larsen[35], C. Lederer-Woods[26], J. Lerendegui-Marco[23], S. Lo Meo[6,7], S.J. Lonsdale[26], M. Lugaro[36], D. Macina[4], A. Manna[7,37], T. Martínez[8], A. Masi[4], C. Massimi[7,37], P.F. Mastinu[38], M. Mastromarco[1], F. Matteucci[2,39], E. Maugeri[27], A. Mazzone[1,40], E. Mendoza[8], V. Michalopoulou[25], F. Mingrone[4], A. Musumarra[9,10], A. Negret[31], R. Nolte[41], F. Ogállar[42], A. Oprea[31], N. Patronis[28], A. Pavlik[43], J. Perkowski[11], L. Piersanti[19,24], I. Porras[42], J. Praena[42], J.M. Quesada[23], D. Radeck[41], D. Ramos Doval[12], R. Reifarth[32], D. Rochman[27], C. Rubbia[4], M. Sabaté-Gilarte[23,4], A. Saxena[44], D. Schumann[27], A.G. Smith[16], N. Sosnin[16], A. Stamatopoulos[25], J.L. Tain[13], Z. Talip[27], A.E. Tarifeño-Saldivia[22], L. Tassan-Got[4,12,25], P. Torres-Sánchez[41], A. Tsinganis[4], J. Ulrich[27], S. Urlass[45], G. Vannini[7,37], V. Variale[1], P. Vaz[29], A. Ventura[7], V. Vlachoudis[4], R. Vlastou[25], A. Wallner[46], P.J. Woods[26], T.J. Wright[16], P. Žugec[17]

[1] Istituto Nazionale di Fisica Nucleare, Bari, Italy
[2]Istituto Nazionale di Fisica Nucleare, Trieste, Italy
[3]European Commission, Joint Research Centre (JRC), Geel, Belgium
[4]European Organization for Nuclear Research (CERN), Switzerland
[5]Charles University, Prague, Czech Republic
[6]Agenzia nazionale per le nuove tecnologie, l'energia e lo sviluppo economico sostenibile (ENEA), Bologna, Italy
[7]Istituto Nazionale di Fisica Nucleare, Bologna, Italy
[8]Centro de Investigaciones Energéticas Medioambientales y Tecnológicas (CIEMAT), Spain
[9]Istituto Nazionale di Fisica Nucleare, Laboratori Nazionali del Sud, Catania, Italy
[10]Dipartimento di Fisica e Astronomia, Università di Catania, Italy
[11]University of Lodz, Poland
[12]IPN, CNRS-IN2P3, Univ. Paris-Sud, Université Paris-Saclay, F-91406 Orsay Cedex, France
[13]Instituto de Física Corpuscular, CSIC - Universidad de Valencia, Spain
[14]Technische Universität Wien, Austria
[15]CEA Saclay, Irfu, Université Paris-Saclay, Gif-sur-Yvette, France
[16]University of Manchester, United Kingdom
[17]Department of Physics, Faculty of Science, University of Zagreb, Croatia
[18]University of York, United Kingdom
[19]Istituto Nazionale di Fisica Nazionale, Perugia, Italy
[20]Dipartimento di Fisica e Geologia, Università di Perugia, Italy
[21]University of Santiago de Compostela, Spain
[22]Universitat Politècnica de Catalunya, Spain
[23]Universidad de Sevilla, Spain
[24]Istituto Nazionale di Astrofisica - Osservatorio Astronomico d'Abruzzo, Italy
[25]National Technical University of Athens, Greece
[26]School of Physics and Astronomy, University of Edinburgh, United Kingdom
[27]Paul Scherrer Institut, Villigen, Switzerland
[28]University of Ioannina, Greece

Abstract The cross section of the ^{89}Y(n,γ) reaction has important implications in nuclear astrophysics and for advanced nuclear technology. Given its neutron magic number N=50 and a consequent small neutron capture cross section, ^{89}Y represents one of the key nuclides for the stellar *s*-process. It acts as a bottleneck in the neutron capture chain between the Fe seed and the heavier elements. Moreover, it is located at the overlapping region, where both the weak and main *s*-process components take place. ^{89}Y, the only stable yttrium isotope, is also an important component of structural materials used in traditional and advanced nuclear reactors. Neutron capture and transmission measurements were performed at the time-of-flight facilities n_TOF at CERN and GELINA at JRC-Geel. Resonance parameters of individual resonances were extracted from a resonance analysis of the experimental transmissions and capture yields, up to a neutron incident energy of 95 keV. Even though a comparison with results reported in the literature shows differences in resonance parameters, the present data are consistent with the Maxwellian averaged cross section suggested by the astrophysical database KADoNiS.

PACS 25.40.Lw · 25.70.Ef · 27.60.+j · 97.10.Cv

1 Introduction

1.1 Astrophysical relevance of ^{89}Y

The elements from iron to uranium are dominantly produced by neutron capture processes, that occur during quiescent stellar evolution or in dramatic scenarios as stellar explosions or neutron star mergers. The explosive nucleosynthesis is characterized by complex reaction networks involving short-lived and very neutron-rich nuclei in presence of high temperatures ($T > 1$ GK) and high neutron densities ($n_n > 10^{20}$ cm^{-3}). The time scale between subsequent neutron captures is of the order of ms; accordingly, this process is known as rapid neutron capture process (*r*-process) [1,2,3]. On the other hand, slow neutron capture processes (*s*-process) operate in environments at low neutron densities ($n_n \approx 10^7 - 10^{11}$ cm^{-3}) in burning phases of stars [4,5]. Here, the times between subsequent neutron capture reactions are larger than the half-lives of β-unstable nuclei and the reaction path follows closely the valley of stability. The *s*-process is commonly divided in two components. Elements with mass number between about 60 and 90 are mainly produced by the weak *s*-process component, that occurs in massive stars during He core burning at temperatures around 0.3 GK, and during C shell burning at around 1 GK [6,7]. The main *s*-process component takes place during the thermal pulsing phase in low-mass Asymptotic Giant Branch (AGB) stars [8], at temperatures around $0.1 - 0.3$ GK. The abundances of elements with 88<A<208 depend on this *s*-process component. Finally, low-metallicity AGB stars are responsible for the production of Pb. The nuclides with neutron magic numbers along the *s*-process path play an important role because they act as bottlenecks given their small (n, γ) cross sections. As a consequence, *s*-process produces three main peaks in the elemental abundance distribution. The first *s*-process peak is due to ^{88}Sr, ^{89}Y, and ^{90}Zr having a magic number of neutrons equal to 50. Hence, the cross section of these nuclides strongly influences the production of all heavier elements (at least) up to the second *s*-process peak, corresponding to the next bottleneck at ^{138}Ba, ^{139}La, and ^{140}Ce with a neutron magic number of 82 (the third peak is represented by ^{208}Pb).

This means that the neutron-capture cross section of ^{89}Y does not only influence the abundance of yttrium itself, but also the abundance distribution of heavier elements. The abundance of yttrium in stars is relatively easy to derive from high-resolution spectra thanks to a large number of strong optical lines, which ensures that a number of them are always available, depending on the spectral coverage. As a consequence, yttrium has been used extensively to constrain stellar models [9] and even astrophysical scenarios [10,11]. A precise and accurate determination of the ^{89}Y neutron capture cross section is a premise to investigate these topics.

1.2 Role of ^{89}Y in advanced nuclear technologies

Apart from the impact on nuclear astrophysics the neutron capture cross section of ^{89}Y is of interest for advanced nuclear technology. Yttrium-hydride offers advantages as a moderator for high temperature thermal nuclear reactors. In contrast to other hydrides considered as moderators, this material retains its relatively high content of hydrogen even at high temperatures considered for these reactors ($850 - 1150\,^{\circ}$C). In addition, its thermal conductivity is excellent [12]. Moreover, yttrium is also proposed as part of inert matrix fuel (IMF). Different concepts have been developed during the last decade to transmute transuranic elements (to reduce their amount in the nuclear waste) using uranium-free IMF in a once-through-cycle. For today's Light Water Reactors yttrium stabilised zirconia and other oxides like alumina, spinel or ceria have been proposed as inert matrix materials. By employing IMF, a larger fraction of plutonium can potentially be consumed in comparison with MOX fuels without breeding new plutonium [13]. Yttrium is also a candidate for the

realization of super-magnets in fusion reactors [14].

1.3 Overview of data reported in the literature

The first high resolution time-of-flight transmission measurements were performed by Morgenstern *et al.* [15] at the 100 m and 200 m transmission stations installed at the 45 MeV electron linear accelerator at Saclay [16]. Neutrons were detected using a 3 cm thick ^{10}B sample surrounded by 8 NaI scintillators. Transmission data were obtained with two samples of Y_2O_3 oxide powder with an areal density of 0.00458 at/b and 0.180 at/b *et al.* [15]. From these data, the resonance energy and strength (i.e. $g\Gamma_n$, where g is the statistical spin factor and Γ_n the resonance neutron width) were derived for 27 resonances between 2 keV and 30 keV. A parity assignment for 9 s-wave resonances and 17 p-wave resonances was made based on the shape of the transmission profile. No details about the R-matrix formalism/approximation that was applied are given.

Later, Camarda [17] reported results from time-of-flight measurements at a 250 m transmission station installed at the Lawrence Livermore Laboratory 100 MeV electron linear accelerator using a ^{6}Li glass scintillator. Transmission data were obtained with 99.9% pure yttrium samples with an areal density of 0.0392 at/b, 0.0840 at/b, and 0.167 at/b. No details about the material form, i.e. metallic or powder, are available in Ref. [17]. From these data the resonance energy and strength for 161 resonances with an energy between 27 keV and 240 keV were derived based on a Single-Level Breit-Wigner approach. A parity assignment for 34 s-wave resonances and 119 p-wave resonances was made based on the shape of the transmission profile. In addition, a resonance shape analysis resulted for 26 s-waves in a spin assignment $J = 0$ or $J = 1$. For p-wave resonances only the separation between $J = 0$ and $J = (1, 2)$ could be made. This resulted in a $J = 0$ assignment for 4 p-wave resonances.

The most extensive study is the work of Agrawal *et al.* [18]. Resonance parameters were derived from an analysis of transmission data obtained from measurements at a 200 m station of the time-of-flight facility ORELA using a 2.54 cm thick sample of yttrium metal. The electron burst width was 5 ns. A proton recoil plastic scintillator was used for neutron energies above 20 keV. For energies below 20 keV, the transmission data obtained with a ^{6}Li glass scintillator were analysed. The resonance energy, strength, and parity for 144 s-wave and 524 p-wave resonances between 10 keV and 740 keV were derived from a resonance shape analysis applying a multilevel-multichannel formalism. A spin assignment for 100 s-wave and 337 p-wave resonances was made. For the resonances with an energy below 10 keV reference is made to Ref. [19], however, it is not clear where the parameters therein are taken from. Agrawal *et al.* [18] found a good agreement with the results of Morgenstern et al. [16] and the resonance energies of Camarda [17]. They observe that the neutron widths for s-wave resonances of Camarda [17] are in general smaller with differences of up to a factor 2. These differences in resonance strength could be due to an incorrect background determination or differences in sample properties or resonance analysis formalisms. Unfortunately, no details about the background correction are given by Morgenstern *et al.* [15], Camarda [17] and Agrawal *et al.* [18], in particular how the impact of the sample on the background level for a sample-in measurement was taken into account (see e.g. Ref. [20]).

For energies below 10 keV, resonance parameters (i.e. resonance energy, strength, spin, and parity) were derived by Raman *et al.* [21] from transmission measurements at a 80 m station and γ-spectroscopic measurements at a 10 m station of ORELA.

Boldeman *et al.* [22] performed capture cross section experiments at a 40 m flight path station of ORELA. They applied the total energy detection principle using C_6F_6 detectors combined with the weighting function and derived capture kernels for resonances with energies below 47 keV. The energy distribution of the incident neutron beam was determined in parallel with a thin ^{6}Li glass scintillator. Capture kernels $K = g\Gamma_n\Gamma_\gamma/(\Gamma_n + \Gamma_\gamma)$, with Γ_γ the radiative width, were derived for 56 resonances after self-shielding and multiple interaction corrections. In case the neutron width dominated the observed resonance width, the spin was derived using the resonance strength reported by Morgenstern *et al.* [15]. By comparing the observed radiative width for the 3.38 keV resonance with the average radiative width for s-wave resonances they assigned this resonance as a s-wave in contrast to a previous p-wave assignment by Morgenstern *et al.* [15]. The p-wave assignment of the 3.38 keV resonance was confirmed by a careful analysis of the thin and thick transmission data of Raman *et al.* [21].

Resonance parameters for neutron interactions with ^{89}Y recommended in the main nuclear data libraries are the result of a compilation of parameters reported in the literature. They are not based on an evaluation procedure involving a resonance shape analysis of time-of-flight cross section data. The parameters in JENDL-5.0 [23] are based on those reported by Boldeman *et al.* [22] and Agrawal *et al.* [18]. The parameters in JEFF-3.3 [24] are taken from ENDF/B-VIII.0 [25]. In the header of the ENDF/B-VIII.0 file reference is made to the 2006 compilation of Mughabghab [26]. For the parameters of

this compilation [26], which are the same as those of the 2018 compilation [27], the main references are the work of Agrawal *et al.* [18] and Boldeman *et al.* [22]. In ENDF/B-VIII.0 resolved parameters are given up to 47 keV, while in JENDL-5.0 up to 100 keV without specifying how the radiative widths for resonances between 47 keV and 100 keV were determined. Although for energies below 47 keV all these compilations, i.e. JENDL-5.0 [23], ENDF/B-VIII.0 [25] and Mughabghab [26] refer to the same experimental data differences between the parameters are present. E.g. for resonances, which were only observed in the capture data of Boldeman *et al.* [22], different neutron widths are recommended in JENDL-5.0 compared to those in ENDF/B-VIII.0. No information is given on how the neutron widths were derived.In addition, a detailed comparison of the resonance parameters reported in the literature and those recommended in the evaluated data libraries reveals obvious clerical mistakes. They are specified in Appendix A. Unfortunately, only the transmission data of Agrawal *et al.* [18] and Raman *et al.* [21] are stored in the EXFOR data library. No capture yield data are available in EXFOR to perform a new evaluation based on a resonance shape analysis of transmissions and capture yields combined with cross section data at thermal energy, i.e. at 25.3 meV.

Maxwellian-averaged capture cross sections (MACS) are spectrum averaged cross sections, which are required for a quantitative description of the *s*-abundances produced during different phases of stellar evolution [28]. They can be derived from the energy dependent capture cross section and Maxwellian neutron energy distribution for a given kT, with k the Boltzman constant and T the temperature. They can also be directly measured in a spectrum that is similar to such a distribution. MACS at the energy of $kT = 30$ keV published in the literature span from 13.5 mb [22] to 19 mb [29], considering data coming from neutron time-of-flight measurements (energy dependent data) [22,30] or activation experiments at a neutron beam with a Maxwellian like distribution [29]. MACS for $kT = 30$ keV extracted from cross sections recommended in evaluated data libraries [23,25] vary from 17 to 21 mb. Even larger differences come from theoretical predictions, where values from 16.6 mb [31] to 88.4 mb [32] are suggested. A list of experimental, evaluated and theoretical values can be found in the astrophysical database KADoNiS [33].

The discussion above suggests that to improve the resonance parameters for neutron interactions with ^{89}Y additional experimental data are required. Transmission data are needed to clarify the differences between the results of Camarda [17] and Agrawal *et al.* [18]. Capture cross section data are required to verify the results of Boldeman *et al.* [22], derive capture kernels for neutron energies above 47 keV and provide capture yields for a resonance shape analysis.

A neutron capture measurement was performed at the 185.2 m long flight path of the CERN n_TOF facility [34,35], while a transmission measurement and an additional capture measurement were completed at the GELINA facility [36,37] of the Joint Research Center (JRC) in Geel (Belgium). From these data resonance parameters for neutron incident energies up to 95 keV were derived. Details of the measurements are described in Sec. 2 and the data reduction procedures in Sec. 3. The results of a resonance shape analysis are discussed in Sec. 4; the Maxwellian-averaged capture cross sections in Sec. 5 and conclusions are drawn in Sec. 6.

2 Experimental details

One of the neutron capture experiments was performed at the CERN n_TOF facility [34], where neutrons are produced by spallation reactions of a 20 GeV/c pulsed proton beam hitting a massive lead block. Charged particles are removed from the neutron beam by a 1.5 T sweeping magnet, and neutrons and ultra-relativistic particles outside the beam line are suppressed by heavy concrete walls and a massive iron shielding 3.5 m in thickness. With a conversion ratio of about 300 neutrons per proton, each beam pulse of 7×10^{12} protons produces a neutron fluence of 10^5 cm^{-2} at the sample position, i.e. at 185.2 m from the spallation target. The resulting neutrons are produced in a wide energy range, from thermal up to 1 GeV. The neutron beam is shaped by two collimators, the second placed close to the last shielding wall in front of the experimental area. The 18 mm aperture of the second collimator gives rise to a nearly symmetric Gaussian-shaped beam profile at the sample position. Thanks to the long flight path and to the short proton pulse width of 7 ns, the resolution in neutron energy is better than 0.5% in the range of the present measurement, i.e. below 95 keV. The energy distribution of the neutron beam was determined relative to the ^{235}U(n,f) cross section by means of a calibrated fission chamber from PTB Braunschweig [38]. During the measurement the intensity of the neutron beam was checked online by a low mass ^{6}Li neutron monitor [39].

Transmission and capture measurements were performed at the GELINA facility [36,37] at JRC-Geel. It is a multi-user facility, featuring a white neutron source with a neutron energy range from 10 meV to 20 MeV. The linear accelerator provides a pulsed electron beam with a maximum energy of 150 MeV, a maximum peak current of 10 A and a repetition rate rang-

ing from 50 to 800 Hz. The measurements presented in this work were performed with the accelerator operating at 800 Hz. A compression magnet reduces the width of the electron pulses to about 2 ns [40]. The electron beam hits a mercury-cooled uranium target producing Bremsstrahlung and subsequently neutrons via photonuclear reactions [41]. Two water-filled beryllium containers mounted above and below the neutron production target are used to moderate the neutrons. The neutron production rate is monitored by BF_3 proportional counters which are mounted on the ceiling of the target hall.

The transmission experiments were performed at a 50-m GELINA measurement station of flight path forming an angle of 9° with respect to the normal to the face of the moderator [42]. The moderated neutron spectrum was used. A shadow bar made of Cu and Pb was placed close to the uranium target to reduce the intensity of the γ-ray flash and the fast neutron component. The neutrons scattered from the moderators were collimated into the flight path through an evacuated aluminium pipe of 50 cm diameter with annular collimators, consisting of borated wax, copper and lead. A set of Pb, Ni and Cu annular collimators were used to reduce the neutron beam to a diameter of 45 mm at the sample position. Additional Li and B_4C collimators were installed to absorb scattered neutrons. A ^{10}B overlap filter was placed close to the neutron target to minimize the contribution of slow neutrons coming from previous accelerator bursts. Close to the sample position, Na, Co, and W black resonance filters were mounted in independent and automatic filter changers to determine the background contribution at 2850 eV, 132 eV, and 18 eV, respectively, and to obtain its time dependence. The Co filter was permanently in the beam to continuously monitor the background level and to account for the impact of the sample or other filters placed in the beam [20]. The neutron beam passing through the sample and filters was further collimated and detected by a cylindrical NE912 Li-glass scintillator (6.35 mm in thickness, 151.6 mm diameter). The scintillator was connected through a boron-free quartz window to a 127 mm EMI 9823 KQB photomultiplier (PMT), which was installed outside the neutron beam perpendicular to its axis. The detector was placed at about 47 m from the neutron target and the diameter of the neutron beam at the detector position was about 90 mm.

At GELINA, the capture measurements were performed at a 60 m station of a flight path, that forms an angle of 9° with respect to the normal to the moderatore face viewing the flight path [43]. The moderated neutron beam was collimated to 75 mm in diameter at the sample position. A ^{10}B anti-overlap filter was placed in the beam to absorb slow neutrons from a previous burst. Black resonance filters (Na and Co) were used to monitor the background during the measurement and to reduce bias effects related to background corrections. The energy distribution of the neutron beam was measured simultaneously with a ^{10}B Frisch gridded ionisation chamber placed at 80 cm before the sample. The chamber was operated with a continuous flow of a mixture of argon (90%) and methane (10%) at atmospheric pressure. The detector consisted of three back-to-back layers of ^{10}B with a total areal density of 1.3x10$^-$5 at/b. The ^{10}B layers, with an effective diameter of 84 mm and areal density of about 0.042 at/b, were evaporated back-to-back on a 30-μm thick aluminium backing and the entrance and exit windows of the chamber had a thickness of 40 μm.

C_6D_6-based liquid scintillators were used for the capture measurements at both n_TOF and GELINA. At n_TOF and GELINA four detectors were placed at an angle of 125° with respect to the direction of the beam. This geometry minimizes systematic effects due to the anisotropy in the primary γ-ray emission from capture of neutrons with $\ell > 0$ [20,43]. Deuterated benzene (C_6D_6) was chosen for its very small neutron sensitivity, given that deuterium and carbon have very low neutron capture cross sections. The detection probability of scattered neutrons was further reduced by coupling each scintillator to a boron-free quartz windowed photomultiplier. To derive the experimental capture yield,i.e. the fraction of incident neutron beam undergoing a (n,γ) reaction in the sample, the total energy detection principle was applied. The principle relies on the use of a low efficiency detection system and a γ-ray detector with a detection efficiency that is proportional to the energy of the incident γ-ray [20]. The latter is realised by applying the pulse height weighting technique (PHWT), which was suggested by Maier-Leibnitz and first applied by Macklin and Gibson [44]. The weighting functions for the detection systems at n_TOF and GELINA were derived by Monte Carlo simulations as described in Ref. [45] and [43], respectively. For both systems the discriminator threshold on the observed deposited energy was taken into account in the calculation of the weighting function. This threshold was 200 keV at n_TOF and 250 keV at GELINA.

Metallic samples of different shape and thickness were used. The samples used in the capture experiments were of cylindrical shape and their characteristics are given in Table 1. For the transmission measurements different layers of squared foils (each an area of 50×50 mm^2, thickness of 0.64 mm and mass of 7.175 g) were used together with a thick disk-shaped sample.

Four different sample combinations were used as described in Table 2. The thick disk sample has a 99.9% purity, while all others present a contamination of 0.5% of Ta and Ho. Normalization of the capture data required additional samples (Au at n_TOF, Fe at GELINA) of the same diameter as the yttrium sample. In addition, ^{nat}C and ^{nat}Pb samples were used to evaluate the background components. The samples and detectors were placed in air conditioned rooms to keep them at a temperature of about 20 °C.

Table 1 Characteristics of ^{89}Y disc samples used in capture measurements

	Diameter (mm)	Thickness (mm)	Mass (g)	Areal density (10^{-3} at/b)
n_TOF	20.0 (1)	1.0	3.161 (1)	3.0291 (8)
GELINA	80.0 (1)	2.0	43.432 (1)	5.8360 (7)

Table 2 Characteristics of ^{89}Y samples used in transmission measurements

Target shape	Areal density (10^{-3} at/b)
2 squared layers	3.8140 (7)
Thick disk	5.8360 (7)
2 squared layers + thick disk	9.650 (1)
7 squared layers	13.352 (2)

3 Data reduction

The experimental transmission $T(t)$ was obtained from the ratio of a sample-in, $C_{in}(t)$, and a sample-out measurement, C_{out}(t), both corrected for their background contributions $B_{in}(t)$ and $B_{out}(t)$, respectively:

$$T(t) = N_t \cdot \frac{C_{in}(t) - B_{in}(t)}{C_{out}(t) - B_{out}(t)}. \quad (1)$$

To avoid systematic effects due to slow variations of both the beam intensity and detector efficiency as a function of time, data were taken by alternating sample-in and sample-out measurements in cycles of about 600 seconds. Such a procedure reduces the uncertainty on the normalization N_t to the beam intensity to less than 0.25% [20]. This uncertainty was evaluated from the ratio of counts in the Li-glass transmission detector and in the BF_3 proportional counters monitoring the intensity of the neutron production in the target hall.

The background in transmission as a function of TOF was parameterized by an analytical expression consisting of a constant and three exponentials [20,42].

$$B(t) = a_0 + a_1 e^{-\lambda_1 t} + a_2 e^{-\lambda_2 t} + a_3 e^{-\lambda_3 (t+\tau_0)} \quad (2)$$

The first exponential is due to the detection of 2.2 MeV γ-rays from neutron capture in hydrogen present in the moderator. The second exponential originates predominantly from neutrons scattered inside the detector station. The third one is due to slow neutrons from previous accelerator cycles; τ_0 is related to the frequency of the accelerator (2.5 ms in the present case, corresponding to the used accelerator frequency of 400 Hz). The free parameters in the analytical expression were determined by a least square fit to saturated resonance dips observed in the TOF-spectra resulting from measurements with black resonance filters.

The experimental capture yield $Y_{exp}(t)$ as a function of time-of-flight t was deduced as:

$$Y_{exp}(t) = \frac{N_c}{S_n + E_n(t)\frac{m_Y}{m_n+m_Y}} \frac{C_w(t) - B_w(t)}{\varphi(t)}, \quad (3)$$

where C_w is the dead time corrected weighted C_6D_6 response, B_w the corresponding background contribution, E_n is the kinetic energy of the incident neutron, S_n is the neutron separation energy, N_c is a normalization factor and φ the energy distribution of the incident neutron beam. The atomic mass of the neutron and target nucleus are denoted by m_n and m_Y, respectively.

The background contribution $B_w(t)$ of the C_6D_6 detectors was expressed as [20]:

$$B_w(t) = b_0 + C_{w,0}(t) + R_n(t)\left(C_{w,C}(t) - C_{w,0}(t)\right), \quad (4)$$

where b_0 is a time-independent contribution, $C_{w,0}(t)$ and $C_{w,C}(t)$ are the weighted TOF spectra from measurements with no sample and with an almost purely scattering natural carbon sample, respectively. The spectra $C_{w,0}(t)$ and $C_{w,C}(t)$ were obtained using the weighting function calculated for the ^{89}Y sample. They were normalized to the same integrated neutron intensity and corrected for the time independent background beforehand. The correction factor $R_n(t)$ is the ratio of the neutron scattering yield of the Y and C sample.

The normalization factor N_c in Eq. (3) accounts for TOF independent quantities such as the absolute intensity of the incident neutron beam, the effective sample area seen by the neutron beam, the absolute detection efficiency, and the solid angle subtended by the sample and the C_6D_6 detectors. This normalization was performed by means of the saturated resonance technique [46,47] using the 4.9 eV resonance in ^{197}Au and the 1.151 keV resonance in ^{56}Fe, at n_TOF and GELINA, respectively. The final uncertainty due to this normalisation, including systematic effects due

to the PHWT, is about 2% at GELINA and 3.52% at n_TOF.

The AGS (Analysis of Geel Spectra) package [48] was used to process the GELINA data and derive the experimental transmissions and capture yields. This package, which is available from the OECD/NEA data bank [49], includes all basic spectrum operations and performs a full uncertainty propagation accounting for both correlated and uncorrelated uncertainty components starting from uncorrelated uncertainties due to counting statistics of the TOF-spectra. The AGS formalism, which results in a substantial reduction of space for data storage, is recommended by the International Nuclear Data Committee (INDC) to store experimental data in the EXFOR data base [50].

4 Results of a resonance shape analysis

Resonance parameters were derived from a resonance shape analysis of the experimental data based on the Reich-Moore approximation [51] of the $\mathcal{R}$-matrix formalism [52]. The transmissions and capture yields obtained from the measurements at GELINA were used to derive parameters for individual resonances with an energy below 95 keV using REFIT [53]. These parameters were verified by an analysis of the capture yield determined at n_TOF using SAMMY [54]. Both REFIT and SAMMY are resonance shape analysis codes which account for experimental effects such as Doppler broadening, neutron self-shielding and multiple interaction, the response function of the TOF-spectrometer and sample impurities.

The initial parameters including an effective scattering radius of 6.7 fm were taken from the ENDF/B-VIII.0 library. The free gas model, with an effective temperature of T_{eff} = 300 K, was applied to account for the thermal motion of the sample atoms. The flight path length of the capture system at GELINA was adjusted fixing the distance for the transmission data to L = 47.669(4) m. This distance was derived from previous transmission experiments at the same measurement station using the parameters recommended by Derrien *et al.* [55]. The final parameters adjusted to the GELINA data are given in Table 4.

For 86 resonances the resonance energy E_R, capture kernel K_γ and resonance strength $g\Gamma_n$were derived. For the other 26 resonances only the capture kernel was adjusted fixing the neutron width to the one defined by the initial parameters. For some resonances it was possible to assign the spin and/or parity. For these resonances the neutron Γ_n and radiation width Γ_γ were derived. The quality of the fits is demonstrated in Figs. 1, 2, 3 and 4, which compare the experimental and calculated transmissions and capture yields in the region of the resonances at 5.71, 9.74, 13.01, 15.2 and 23.04 keV. Fig. 1 illustrates problems with the resonance parameters in the evaluated data libraries for the resonances at 5.71 and 13.0 keV. Fig. 2 shows the capability to determine the neutron angular momentum ℓ for the resonance at 9.74 keV. A significant better fit is obtained supposing $\ell = 0$, as in JENDL-5.0 [23]), comparhttps://www.overleaf.com/project/625415879e4923314d2b9d09ed to the $\ell = 1$ assignment recommended in ENDF/B-VIII.0 [25] and Mughabghab [26]. Unfortunately, for this resonance the spin can not be unambiguously assigned. Fig.3 shows the data in the region of the *p*-wave resonance at 23.0 keV. This figure shows a clear difference in the quality of the fit for a J=2 assignment as in ENDF/B-VIII.0 [25] and Mughabghab [26] compared to the J=1 assignment recommended in JENDL-5.0[23]. Fig. 4 shows the results for the resonance at 15.2 keV. This resonance was assigned J=0, ℓ=0 by Agrawal *et al.* [18] while Morgenstern *et al.* [15] assumes a spin J = 1 for this s-wave resonance. Fig. 4 reveals that the best fit is obtained if the resonance is considered as a doublet, with a p-wave resonance (ℓ=1) with spin J = 1 and an s-wave resonance (ℓ=0) with spin J=0. The p-wave character of the 3.38 keV resonance was derived from the transmission profile. This shows that making parity or spin assignments based on the radiative width (or capture kernels) have to be taken with care.

The n_TOF data were used to determine capture kernels for resonances with an energy below 40 keV. In this analysis the neutron width was fixed to the one derived from the fit to the GELINA data, while Γ_γ was adjusted. An example of such an adjustment is shown in the upper panel of Fig. 5. This figure compares for the 9.735 keV and 23.037 keV resonances the capture yield derived at n_TOF with the yield calculated using the radiation width adjusted to the n_TOF data (dashed blue line) and the parameters derived from a fit to the GELINA data (full red line). The capture kernels derived from the n_TOF data are fully consistent with those derived from the experiment at GELINA. This is illustrated in the bottom panel of Fig. 5, which plots the ratio of kernels derived from the n_TOF and GELINA data as a function of the incident neutron energy. The average ratio of the kernels is 1.00, with a standard deviation of 0.05.

As mentioned in the introduction, parameters of individual resonances derived from experimental data were previously reported in Refs. [15,17,18,21,22].

The ratio of the resonance energy derived from Agrawal *et al.* [18] and the one derived from this work is plotted as a

function of neutron energy in Fig.6. No clear energy dependence is observed and the weighted average ratio is 1.00088(2). Therefore, the resonance energies of Agrawal *et al.* [18], which go up to 740 keV, can be corrected by this factor such that they are relative to those reported by Derrien *et al.* [55] for ^{238}U.

Fig. 7 plots the ratio of the resonance strengths of Refs.[15,17,18], Ref.[27] and Refs.[25,23] with the values derived in this work as a function of incident neutron energy. The weighted average ratios are given in Table 3. Fig. 7 together with the data in Table 3 show that within uncertainties there is a good agreement between the strengths derived by Agrawal *et al.* [18] and Morgenstern et al. [16] and those derived in this work. The strengths reported by Camarda[17] are on average lower by almost 25%. The values obtained in this work are closer to those of JENDL-5.0[23] compared those of ENDF/B-VIII.0[25].

The ratio of the capture kernels of Boldeman et al. [22], Mughabghab [27] and the ones derived from JENDL-5.0[23] and ENDF/B-VIII.0[25] with those derived in this work are plotted in Fig. 8. The weighted average ratios are given in Table 3. The results in Fig.8 and Table3 show that there is a very good agreement between the values derived in this work and those of Boldeman *et al.* [22]. The corrections applied by Mughabghab[27] to the capture kernels of Boldeman *et al.* [22] result in kernels that are on average underestimated by about 15%. The capture kernels derived from the JENDL-5.0[23] library are in better agreement with those derived in this work compared to the kernels obtained from the ENDF/B-VIII.0[25] library.

Given the limitations in a clear spin and/or parity assignment for a number of resonances, it is hard to derive accurate average resonance parameters for a given spin and parity group. The number of observed resonances in this work leads to a combined s- and p-wave spacing of about 850 eV (the actual spacing is likely even smaller as we might miss a few weak resonances). This value is significantly smaller compared to the value 1035(30) eV resulting from the s- and p-wave level spacings listed in Mughabghab's compilation [27]. The average radiative widths of s- and p-wave resonances derived from resonances with a firm spin assignment, 139(15) meV and 254(37) meV respectively, are in a reasonable agreement with those in Ref. [27], which are 134 meV and 300 meV.

5 Maxwellian averaged cross section

The abundances produced in the s-process in thermally pulsing low-mass AGB stars can be estimated theoretically using MACS. The temperatures during the

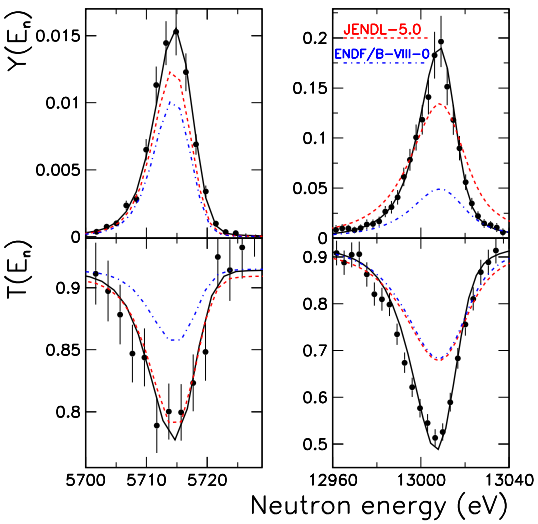

Fig. 1 (Color online) Upper panels: experimental capture yields obtained at GELINA; Lower panels: results of transmission measurements performed at GELINA with the 7 squared layers ^{89}Y sample, see Tab. 2. The results of $\mathcal{R}$-matrix fits are included (black lines); red and blue lines refer to the calculated yields and transmissions using the resonance parameters in JENDL-5.0 [23] and ENDF/B-VIII.0 [25], respectively.

Table 3 Weighted average ratio of the resonance strength $g\Gamma_n$ and capture kernel K reported in Refs. [15,17,18,27,23,25] and the values derived in this work (TW).

DATA,X	$g\Gamma_n$(X)/$g\Gamma_n$(TW)	K(X)/K(TW)
Morgestern et al. [15]	0.96 (3)	
Camarda [17]	0.75 (2)	
Agrawal et al. [18]	0.93 (2)	
Mughabghab [27]	0.96 (1)	0.90 (2)
JENDL-5.0 [23]	0.964 (5)	1.150 (3)
ENDF/VII.0 [25]	0.819 (2)	0.948 (2)

He-shell burning episodes in AGB stars are about 90 and 250 MK, corresponding to energies of $kT = 8$ and 23 keV [28]. This range has to be extended to cover the temperatures during C-shell burning in massive stars corresponding to a kT of about 90 keV.

The MACS calculated from the data obtained in this work are reported in Table 5 and shown in Fig. 9. They were calculated from the capture kernels in Table 4 following the procedure proposed in [56,57]. The contribution from resonances observed in this work were complemented by a $1/v$ contribution that was normalized to a cross section of 1280 (20) mb at 2200 m/s from the 1981 compilation of Mughabghab et al. [27]. This

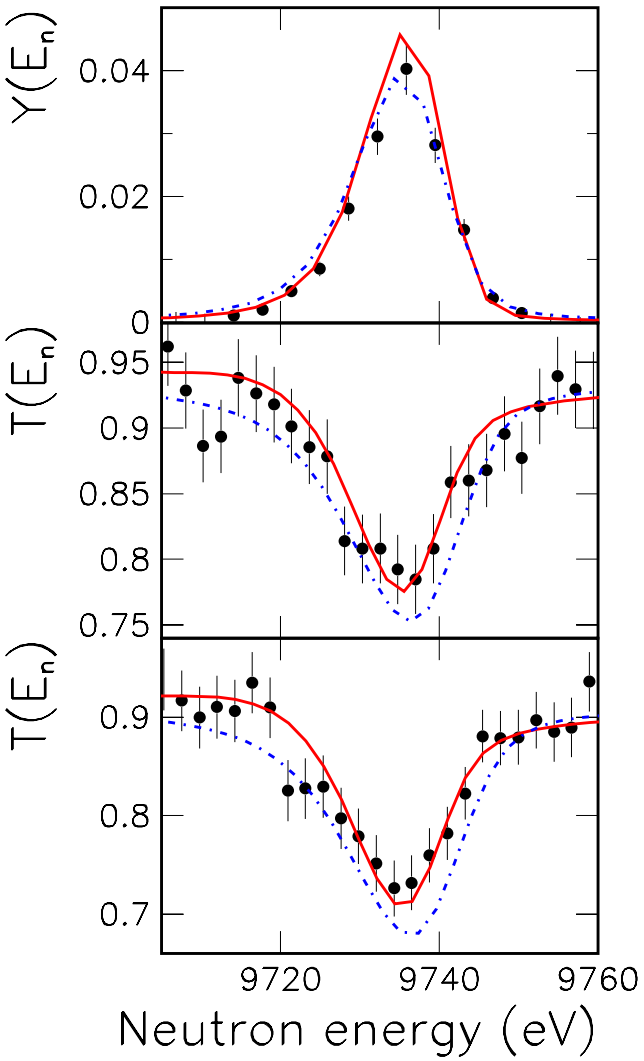

Fig. 2 (Color online) Upper panel: experimental capture yields obtained at GELINA; Lower panels: results of transmission measurements performed at GELINA with the thick disc + 2 squared layers (middle) and the 7 squared layers (lowest panel) ^{89}Y samples, see Tab. 2. The results of $\mathcal{R}$-matrix fits are included. Full red lines refer to a fit with $\ell = 0$, $J = 0$; blue dash-dotted lines to a fit with $\ell = 1$, $J = 0$.

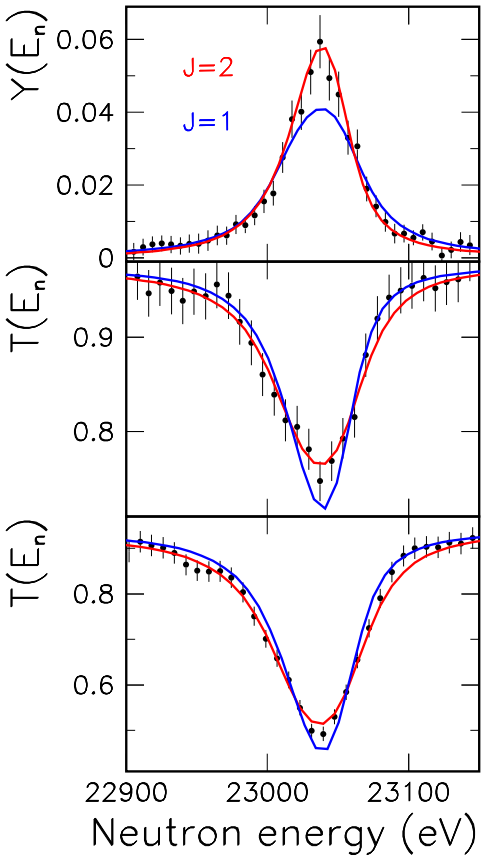

Fig. 3 (Color online) Upper panel: experimental capture yield obtained at GELINA; Lower panels: Results of transmission measurements performed with the 2 squared layers (middle) and the thick disk + 2 squared layers (lowest panel) ^{89}Y samples, see Tab. 2. The results of $\mathcal{R}$-matrix fits are included. See text for the details.

value is given in the 2006 [26] and 2018 compilation [27]. The contribution due to neutron energies above 95 keV was derived from the ^{89}Y(n,γ) cross section in JENDL-5.0 [23]. This contribution, which is specified in Table 5 and Fig. 9, is negligible for $kT \simeq 10$ keV, about 10% for $kT = 30$ keV and 60% for $kT = 90$ keV. A possible p-wave contribution from direct capture has been investigated using an approach similar to that in Ref. [58]. This contribution has been found small, (i.e. 0.5 mb at its maximum for $kT = 100$ keV) and was neglected. The uncertainties in Table 5 are derived by only propagating the uncertainties in Table 4 and an overall uncertainty of 5% for the contribution of incident neutron energies above 95 keV. The uncertainties in Table 4 have to be combined with a normalisation uncertainty of the capture data, which is about 2% [43].

The MACSs for which the contribution from neutron energies lower than 95 keV is estimated to be more than about 97% (i.e. MACS for kT $\leq$ 20 keV) are shown in the right panel of Fig. 9. The values derived from the experiments presented in this work are compared with those derived from the energy dependent cross sections in ENDF/B-VIII.0 [25] and JENDL-5.0l[23]. The best agreement is obtained with the MACS derived from the JENDL-5.0 library. Given the results in Fig. 9 and the discussion on the resonance parameters in section 4, the^{89}Y(n,γ) cross section recommended in JENDL-5.0

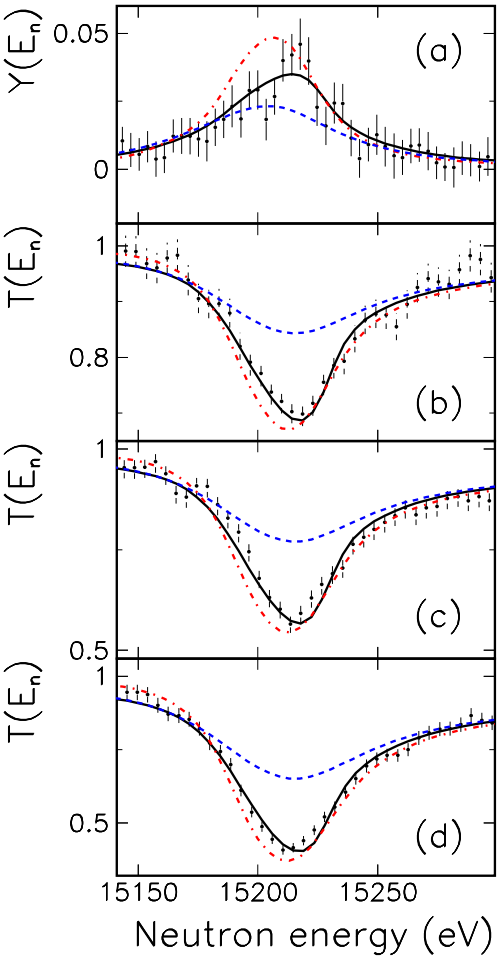

Fig. 4 (Color online) Panel (a): experimental capture yield obtained at GELINA; Lower panels: results of transmission measurements performed at GELINA with 2 squared layers (b), the thick disk (c) and the 7 squared layers (d) ^{89}Y samples, see Tab. 2. The results of $\mathcal{R}$-matrix fits are included. Dash-dotted red lines refer to the fit with $\ell = 0$, $J = 1$; blue dashed lines to $\ell = 0$, $J = 0$; full black lines to the fit with two resonances with $\ell = 0$, $J = 0$ and $\ell = 1$, $J = 1$.

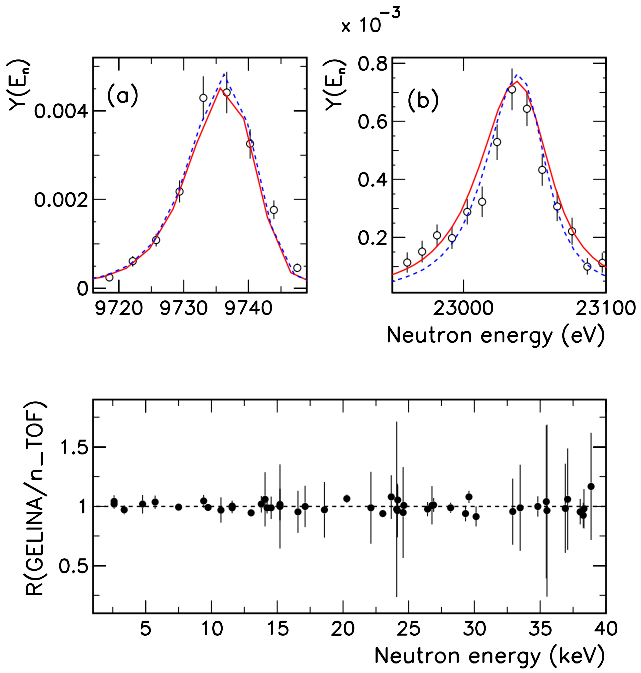

Fig. 5 (Color online) Upper panels: experimental capture yields obtained at n_TOF. The results of $\mathcal{R}$-matrix fits (with the as Γ_γ free parameter) to these yields are represented by a blue dashed line. The red full line is the theoretical yield using the resonance parameters derived from the GELINA data; see text for details. Lower panel: Ratio of the capture kernels extracted from the n_TOF (SAMMY code) and GELINA (REFIT code) data as a function of the resonance energy.

was used to calculate the contribution for neutron energies above 95 keV.

The ratio of the MACS recommended in the KADoNIS data base [33] and those obtained in this work (Table 5) is shown in Fig.10. The recommended MACS are derived from the capture cross section in ENDF/B-VII.1 normalised to the MACS = 20.1 (6) mb at kT = 30 keV. The latter is obtained by correcting the results of activation measurements performed by Käppeler et al. [29] for a bias in the ^{197}Au(n,γ) cross section that was used in Ref. [29] to normalise the data. The MACS at kT = 30 keV differ by about 7% which is almost twice the combined uncertainty of 4.6%. Fig.10 shows that within the uncertainties, which are dominated by those of the recommended values, the MACS reported in this work are consistent with those of Ref. [33].

A stellar model for a 2 M$_\odot$ star, with metallicity representative of the Galactic disk (Z = 0.01), was computed to assess the impact of the MACS determined in this work on the s-process nucleosynthesis in low-mass AGB stars. Then, we compared the corresponding surface distribution to the same model, but computed with the MACS recommended in the KaDoNIS v1.0 database. Simulations were performed with the FuNS code [59], [60], [61]. In low-mass AGB stars, the production of heavy elements mainly proceeds via the capture of free neutrons released by the ^{13}C(α, n)^{16}O reaction. In AGB stars with near-solar metallicity, this reaction can be activated in both radiatively-stable and/or convectively-unstable inner stellar layers (e.g., [62]). The nuclear-processed material is then gradually carried to the stellar surface through recursive mixing episodes, known as third dredge-ups (TDUs, see, e.g., [5]). After each TDU, the stellar envelope becomes increasingly enriched in heavy s-process elements. The neutron burst induced by convective ^{13}C-burning, which occurs at relatively high temperatures (kT 20 keV), may affect the heavy element nucle-

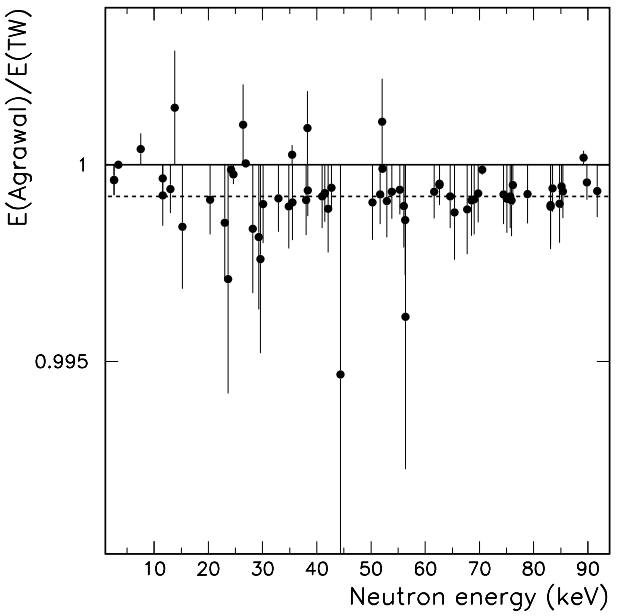

Fig. 6 Ratio of the resonance energy from Ref. [18] and the one derived in this work as a function of the resonance energy energy.

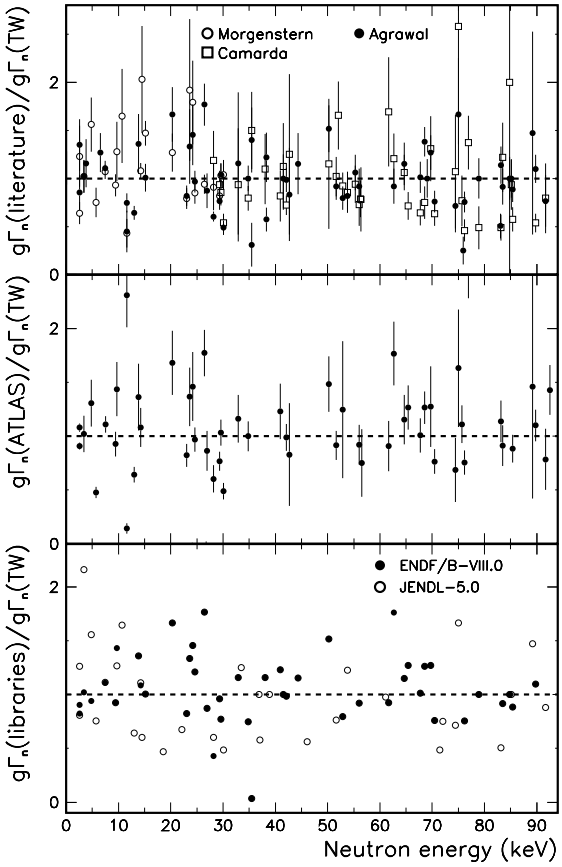

Fig. 7 Upper panel: Ratio of the resonance strength $g\Gamma_n$ from Ref. [15][17][18] and the one derived in this work (TW) (upper panel), from Ref. [27] and the one derived in this work (TW) (center panel), from Ref. [24][23] and the one derived in this work (TW) (bottom panel) as a function of neutron energy.

osynthesis only for the first few TDU episodes. This is clearly visible in the upper panel of Fig.11, which depicts the situation at the 5^{th} TDU episode. While the ^{89}Y production is marginally affected by the adoption of the small changes in the MACS, the surface abundance of heavier isotopes shows a more pronounced decrease. This is due to the lower MACS for ^{89}Y(n,γ) in the energy region where the convective ^{13}C burning occurs. As a consequence, a maximum decrease of about 10% is obtained. This difference, however, is progressively erased through the following AGB phase, during which the neutron burst induced by the main ^{13}C radiative burning, which takes place at lower temperatures (kT $\sim$ 8 keV, see [63]), dominates the heavy element nucleosynthesis. As a matter of fact, variations lower than 5% are found at the last (12^{th}) TDU (lower panel of Fig.11). During late TDUs ,in fact, the production of heavy elements only occurs during the radiative ^{13}C burning, thus at temperatures where the MACS derived in this work confirms previous available data (see Fig.9) and calculation related to AGB stars evolution.

6 Conclusions

High resolution cross section measurements were carried out at the time-of-flight facilities GELINA and n_TOF using metallic samples of ^{89}Y. The REFIT code was used to derive resonance parameters for neutron interactions with ^{89}Y for incident neutron energies up to 95 keV from a simultaneous analysis of transmission and capture yield data. These parameters are fully consistent with the capture yield data derived at n_TOF. Thanks to the combination of experimental data obtained in different experimental conditions at these TOF-facilities, bias effects due to the TOF response function, the normalization of capture data and the background contributions are reduced. The resonance energies and strengths derived in this work are in good agreement with the results of transmission measurements reported

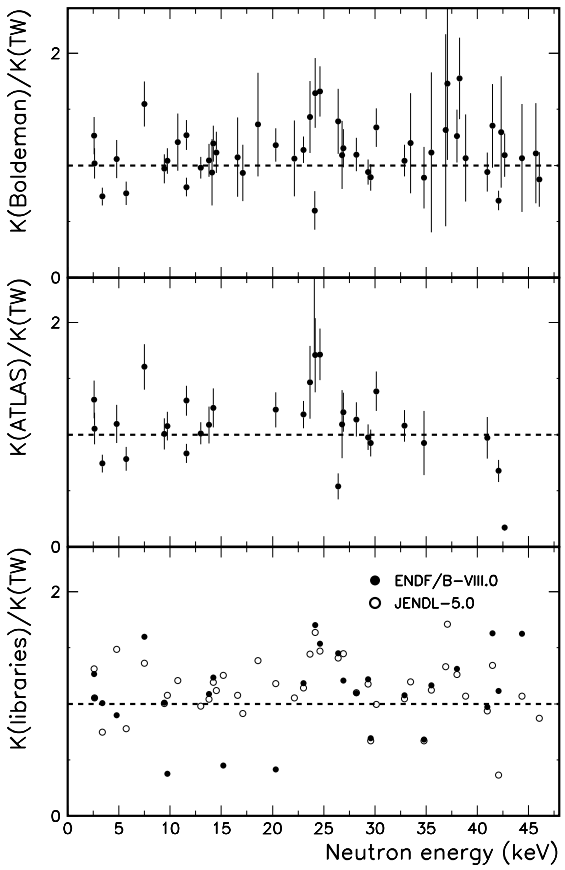

Fig. 8 Ratio of the capture kernel K from Ref. [22] and the one derived in this work (TW) (upper panel), from Ref. [27] and the one derived in this work (TW) (center panel), from Ref. [24][23] and the one derived in this work (TW) (bottom panel)as a function of neutron energy.

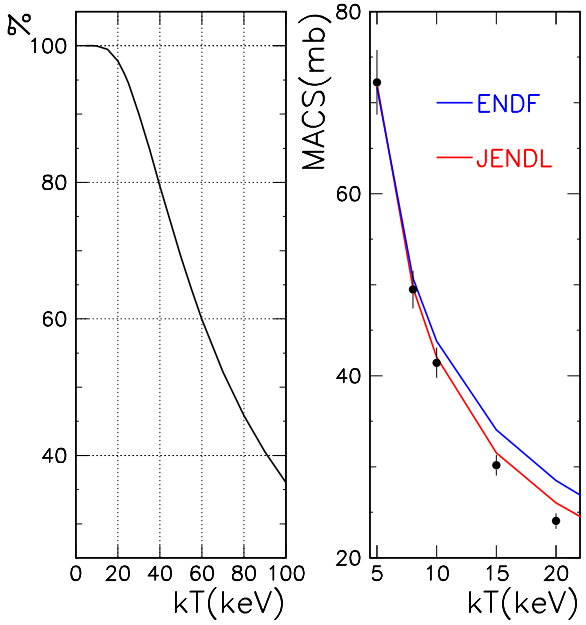

Fig. 9 (Color online) Left panel: Relative contribution of the energy range up to 95 keV to the MACS as a function of thermal energy; Right panel: MACSs as a function of thermal energy, present data (full circles) are compared with the ENDF/B.VIII-0 [25] and JENDL-5.0 [23] libraries.

by Agrawal *et al.* [18]. The capture kernels derived in this work are fully consistent with those resulting from the work of Boldeman *et al.* [22], which are the only capture experiments in the resolved resonance region for ^{89}Y that were reported in the literature. In this work kernels were derived up to an energy of 95 keV, while those in Ref.[22] are limited to 47 keV. Hence, the results obtained in this work together with the transmission data of Agrawal *et al.* [18] and Raman [21], which are up to now the only data available in the EXFOR data library, can be used for a new evaluation of neutron interactions with ^{89}Y based on a resonance shape analysis of traceable experimental data and extend the resolved resonance region.

The capture kernels of the 112 resonances complemented with the ^{89}Y(n,γ) cross section at thermal energy and the one in JENDL-5.0[23] for neutron energies above 95 keV were used to calculated MACS at different temperatures of the Maxwellian distribution. They are within uncertainties consistent with those recommended in the astrophysical database KADoNiS [33] and support the results of stellar model calculations obtained with these recommended values.

Acknowledgements This research was funded by the European Community Seventh Framework Programme FP7/2007-2011 under the Project CHANDA (Grant No. 605203), by the European Commission within HORIZON2020 via the EURATOM project EUFRAT for transnational access and by the funding agencies of the participating institutes.

Appendix A: List of mishaps in evaluated data libraries

In JENDL-5.0 [23]

1. The neutron width Γ_n for the 7483 eV resonance is given as 0.654 eV and should be 65.4 eV.

In ENDF [25] and JEFF-3.3 [24]

1. There is a group of resonances, i.e. the resonances at 51703, 52035, 55330, 56582, 62459, 69070, 74490,

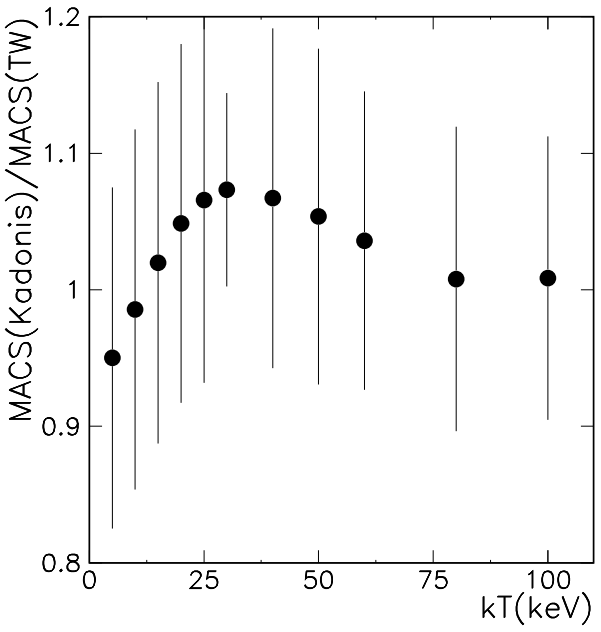

Fig. 10 (Color online) Ratio of the MACS recommended in the KADoNIS library [33] and those obtained in this work as a function of kT. The uncertainties are the combined uncertainties which are dominated by the uncertainties of the recommended values.

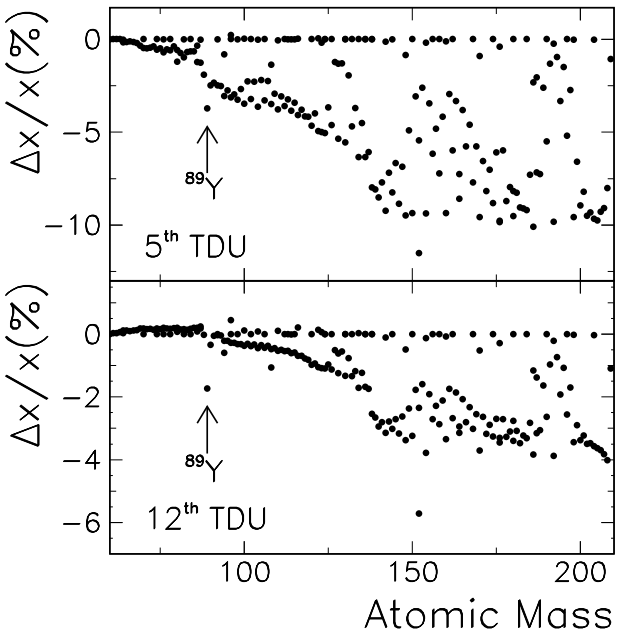

Fig. 11 Percentage isotopic abundance difference between models computed with the MACS of this work and the provided in [33], at the 5^{th} (upper panel) and at the 12^{th} TDU.

75107, 75977, 83180, 85210, 89173, and 94125 eV, with neutron widths that are reduced by a factor 1000, e.g. the Γ_n for the 51703 eV resonance is given as 0.06 eV and should be 60 eV.

2. The energy for the 53865 eV resonance is given as 52865 eV.

References

1. E.M. Burbidge, G.R. Burbidge, W.A. Fowler, F. Hoyle, Synthesis of the elements in stars, Rev. Mod. Phys. **29**, 547 (1957). DOI 10.1103/RevModPhys.29.547
2. J.J. Cowan, C. Sneden, J.E. Lawler, A. Aprahamian, M. Wiescher, K. Langanke, G. Martínez-Pinedo, F.K. Thielemann, Origin of the heaviest elements: The rapid neutron-capture process, Reviews of Modern Physics **93**(1), 015002 (2021). DOI 10.1103/RevModPhys.93.015002
3. F.K. Thielemann, M. Eichler, I.V. Panov, B. Wehmeyer, Neutron Star Mergers and Nucleosynthesis of Heavy Elements, Annual Review of Nuclear and Particle Science **67**, 253 (2017). DOI 10.1146/annurev-nucl-101916-123246
4. M. Busso, R. Gallino, G.J. Wasserburg, Nucleosynthesis in Asymptotic Giant Branch Stars: Relevance for Galactic Enrichment and Solar System Formation, **37**, 239 (1999). DOI 10.1146/annurev.astro.37.1.239
5. O. Straniero, R. Gallino, S. Cristallo, s process in low-mass asymptotic giant branch stars, **777**, 311 (2006). DOI 10.1016/j.nuclphysa.2005.01.011
6. C.M. Raiteri, M. Busso, R. Gallino, G. Picchio, S-process nucleosynthesis in massive stars and the weak component. ii. carbon burning and galactic enrichment, Astrophys. J. **371**, 665 (1991). DOI 10.1086/169932
7. M. Pignatari, R. Gallino, M. Heil, M. Wiescher, F. Käppeler, F. Herwig, S. Bisterzo, The Weak s-Process in Massive Stars and its Dependence on the Neutron Capture Cross Sections, **710**(2), 1557 (2010). DOI 10.1088/0004-637X/710/2/1557
8. R. Gallino, C. Arlandini, M. Busso, M. Lugaro, C. Travaglio, O. Straniero, A. Chieffi, M. Limongi, Evolution and Nucleosynthesis in Low-Mass Asymptotic Giant Branch Stars. II. Neutron Capture and the S-Process, **497**(1), 388 (1998). DOI 10.1086/305437
9. M. Busso, R. Gallino, D.L. Lambert, C. Travaglio, V.V. Smith, Nucleosynthesis and mixing on the asymptotic giant branch. iii. predicted and observed s-process abundances, Astrophys. J. **557**, 802 (2001). DOI 10.1086/322258
10. S. Cristallo, C. Abia, O. Straniero, L. Piersanti, On the need for the light elements primary process (lepp), Astrophys. J. **801**, 53 (2015). DOI 10.1088/0004-637X/801/1/53
11. O. Trippella, M. Busso, E. Maiorca, F. Käppeler, S. Palmerini, Astrophys. J. **787**, 41 (2014). DOI 10.1088/0004-637x/787/1/41
12. NASA Technical Note, NASA TN D-4615 (1968)
13. M. Streit, W. Wiesenack, T. Tverberg, C. Hellwig, B. Oberländer, Yttrium stabilised zirconia inert matrix fuel irradiation at an international research reactor, J.

Nucl. Mat. **352**, 349 (2006). DOI 10.1016/j.jnucmat.2006.02.067
14. N. Yanagi, Y. Terazaki, S. Ito, K. Kawai, Y. Seino, T. Ohinata, Y. Tanno, K. Natsume, S. Hamaguchi, H. Noguchi, H. Tamura, T. Mito, H. Hashizume, A. Sagara, Progress of the design of hts magnet option and r&d activities for the helical fusion reactor, IEEE Trans. App. Supercond. **24**, 4202805 (2014). DOI 10.1109/TASC.2013.2292775
15. J. Morgenstern, R. Alves, J. Julien, C. Samour, Paramètres des résonances et fonctions densités s0 et s1 pour cl, 51v, 89y, zr, la, 141pr et 209bi, Nuclear Physics A **123**, 561 (1969). DOI 10.1016/0375-9474(69)91005-7
16. J. Morgenstern, S. De Barros, A. Bloćh, P. Chevillon, V. Huynh, H. Jackson, J. Julien, C. Lopata, C. Samour, Analyse des paramètres de résonances du cobalt et du manganèse, induites par des neutrons d'énergie inférieure á 120 kev, Nuclear Physics A **102**, 602 (1967). DOI 10.1016/0375-9474(67)90398-3
17. H.S. Camarda, High resolution neutron total cross section measurement of ^{89}Y, Phys. Rev. C **16**, 1803 (1977). DOI 10.1103/PhysRevC.16.1803
18. H. Agrawal, J. Garg, J. Harvey, 89Y + n resonances for E = 10–740 keV and intermediate structure, Nucl. Phys. A **501**, 18 (1989). DOI 10.1016/0375-9474(89)90563-0
19. S.F. Mughabghab, M. Divadeenam, N.E. Holden, *Neutron cross sections* (Elsevier, 1981). DOI 10.1016/B978-0-12-509701-7.X5001-9. Volume 1: Neutron Resonance Parameters and Thermal Cross Sections, Part A: Z=1–60
20. P. Schillebeeckx, B. Becker, Y. Danon, K. Guber, H. Harada, J. Heyse, A.R. Junghans, S. Kopecky, C. Massimi, M.C. Moxon, N. Otuka, I. Sirakov, K. Volev, Determination of Resonance Parameters and their Covariances from Neutron Induced Reaction Cross Section Data, Nucl. Data Sheets **113**, 3054 (2012). DOI 10.1016/j.nds.2012.11.005
21. S. Raman, O. Shahal, A.Z. Hussein, G.G. Slaughter, J.A. Harvey, Enhanced primary dipole transitions in the ^{89}Y(n,γ) reaction, Phys. Rev. C **23**, 1979 (1981). DOI 10.1103/PhysRevC.23.1979
22. J.W. Boldeman, B.J. Allen, A.R. de L. Musgrove, R.L. Macklin, The neutron capture cross section of yttrium-89, Nucl. Sci. Eng. **64**, 744 (1977). DOI 10.13182/NSE77-A27103
23. O. Iwamoto, N. Iwamoto, S. Kuneida, F. Minato, S. Nakayama, Y. Abe, K. Tsubakihara, S. Okumura, C. Ishizuka, T. Yoshida, S. Chiba, N. Otuka, J.C. Sublet, H. Iwamoto, K. Yamamoto, Y. Nagaya, K. Tada, C. Konno, N. Matsuda, K. Yokoyama, H. Taninaka, A. Oizumi, M.F. , S. Okita, G. Chiba, S.K. Satoshi Sato, Masayuki Ohta, Japanese evaluated nuclear data library version 5: JENDL-5, J. Nucl. Sci. Technol. **60**, 1 (2023). DOI 10.1080/00223131.2022.2141903. URL https://wwwndc.jaea.go.jp/jendl/j5/j5.html. https://wwwndc.jaea.go.jp/jendl/j5/j5.html
24. A.J.M. Plompen, et al., The joint evaluated fission and fusion nuclear data library, JEFF-3.3, Eur. Phys. J. A **56**, 181 (2020). DOI 10.1140/epja/s10050-020-00141-9. URL https://www.oecd-nea.org/dbdata/jeff/jeff33/. https://www.oecd-nea.org/dbdata/jeff/jeff33/
25. D.A. Brown, et al., ENDF/B-VIII.0: The 8th Major Release of the Nuclear Reaction Data Library with CIELO-project Cross Sections, New Standards and Thermal Scattering Data, Nucl. Data Sheets **148**, 1 (2018). DOI 10.1016/j.nds.2018.02.001. URL https://www.nndc.bnl.gov/endf/. Special Issue on Nuclear Reaction Data, https://www.nndc.bnl.gov/endf/
26. S.F. Mughabghab, *Atlas of Neutron Resonances* (Elsevier, 2006)
27. S.F. Mughabghab, *Atlas of Neutron Resonances* (Elsevier, 2018). DOI 10.1016/c2015-0-00522-6. Volume 1: Resonance Properties and Thermal Cross Sections Z=1-60
28. R. Gallino, C. Arlandini, M. Busso, M. Lugaro, C. Travaglio, O. Straniero, A. Chieffi, M. Limongi, Astrophys. J. **497**, 388 (1998). DOI 10.1086/305437
29. F. Käppeler, W.R. Zhao, H. Beer, U. Ratzel, 88Sr and 89Y: The s-Process at Magic Neutron Number N = 50, Astrophys. J. **355**, 348 (1990). DOI 10.1086/168769
30. A.R. de L. Musgrove, B.J. Allen, J.W. Boldeman, R.L. Macklin, in *Inter. Conf. Neutron Physics and Nuclear Data for Reactors and other Applied Purposes* (OECD, Paris, 1978), p. 449. URL https://inis.iaea.org/search/searchsinglerecord.aspx?recordsFor=SingleRecord&RN=11524511
31. S. Goriely. Hauser-Feshbach rates for neutron capture reactions (version 8/29/2005) (2005)
32. T. Rauscher, F.K. Thielemann, Astrophysical reaction rates from statistical model calculations, Atomic Data and Nuclear Data Tables **75**, 1 (2000). DOI 10.1006/adnd.2000.0834
33. I. Dillmann, R. Plag, F. Käppeler, A. Mengoni, C. Heinz, M. Pignatari, The new KADoNiS v1.0 and its influence on the weak *s*-process nucleosynthesis, PoS **NIC XIII**, 057 (2015). DOI 10.22323/1.204.0057
34. C. Guerrero, et al., Performance of the neutron time-of-flight facility n_TOF at CERN, Eur. Phys. J. A **49**(2), 27 (2013). DOI 10.1140/epja/i2013-13027-6. URL http://cds.cern.ch/record/1709388
35. U. Abbondanno, et al., CERN n_TOF facility: Performance report. Tech. Rep. CERN-SL-2002-053 ECT, CERN (2003). URL http://cds.cern.ch/record/601511/
36. A. Bensussan, J. Salome, Gelina: A modern accelerator for high resolution neutron time of flight experiments, Nuclear Instruments and Methods **155**, 11 (1978). DOI 10.1016/0029-554X(78)90181-7
37. W. Mondelaers, P. Schillebeeckx, Notizario Neutroni e Luce di Sincrotrone **11**, 19 (2006)
38. C. Borcea, et al., Results from the commissioning of the n_TOF spallation neutron source at CERN, Nucl. Instrum. Methods A **513**, 524 (2003). DOI 10.1016/S0168-9002(03)02072-2
39. S. Marrone, et al., A low background neutron flux monitor for the n_TOF facility at CERN, Nucl. Instrum. Methods A **517**, 389 (2004). DOI 10.1016/j.nima.2003.09.060
40. D. Tronc, J.M. Salomé, K.H. Böckhoff, A new pulse compression system for intense relativistic electron beams, Nucl. Instrum. Methods A **228**, 217 (1985). DOI 10.1016/0168-9002(85)90263-3
41. J.M. Salome, R. Cools, Neutron producing targets at GELINA, Nucl. Instrum. Methods **179**, 13 (1981). DOI 10.1016/0029-554X(81)91156-3
42. I. Sirakov, B. Becker, R. Capote, E. Dupont, S. Kopecky, C. Massimi, P. Schillebeeckx, Results of total cross section measurements for ^{197}au in the neutron energy region from 4 to 108 kev at gelina, Eur. Phys. J. A **49**, 144 (2013). DOI 10.1140/epja/i2013-13144-2
43. A. Borella, G. Aerts, F. Gunsing, M. Moxon, P. Schillebeeckx, R. Wynants, The use of C_6D_6 detectors for neutron induced capture cross-section measurements in the

resonance region, Nucl. Instrum. Methods A **577**, 626 (2007). DOI 10.1016/j.nima.2007.03.034
44. R.L. Macklin, J.H. Gibbons, Capture-Cross-Section Studies for 30–220-keV Neutrons Using a New Technique, Phys. Rev. **159**, 1007 (1967). DOI 10.1103/PhysRev.159.1007
45. U. Abbondanno, et al., New experimental validation of the pulse height weighting technique for capture cross-section measurements, Nucl. Instrum. Methods A **521**, 454 (2004). DOI 10.1016/j.nima.2003.09.066
46. R.L. Macklin, J. Halperin, R.R. Winters, Gold neutron-capture cross section from 3 to 550 keV, Phys. Rev. C **11**, 1270 (1975). DOI 10.1103/PhysRevC.11.1270
47. N. Yamamuro, T. Hayase, T. Doi, Y. Fujita, K. Kobayashi, R.C. Block, Reliability of the weighting function for the pulse height weighting technique, Nucl. Instrum. Methods **133**, 531 (1976). DOI 10.1016/0029-554X(76)90442-0
48. B. Becker, C. Bastian, F. Emiliani, F. Gunsing, J. Heyse, K. Kauwenberghs, S. Kopecky, C. Lampoudis, C. Massimi, N. Otuka, P. Schillebeeckx, I. Sirakov, Data reduction and uncertainty propagation of time-of-flight spectra with ags, Journal of Instrumentation **7**, 11002 (2012). DOI 10.1088/1748-0221/7/11/P11002
49. B. Becker, C. Bastian, J. Heyse, S. Kopecky, P. Schillebeeckx, Ags - analysis of geel spectra users' manual. Tech. Rep. NEA/DB/DOC(2014)4, OECD - NEA (2014). URL https://www.oecd-nea.org/upload/docs/application/pdf/2020-01/db-doc2014-4.pdf
50. F. Gunsing, P. Schillebeeckx, V. Semkova, Exfor data in resonance region and spectrometer response function. Tech. Rep. INDC(NDS)-0647, IAEA (2013). URL https://inis.iaea.org/collection/NCLCollectionStore/_Public/45/037/45037228.pdf?r=1
51. C. Reich, M.S. Moore, R-Matrix Theory of Nuclear Reactions
52. A. Lane, R.G. Thomas, R-Matrix Theory of Nuclear Reactions
53. M.C. Moxon, J.B. Brisland, GEEL REFIT, A least squares fitting program for resonance analysis of neutron transmission and capture data computer code. Tech. Rep. AEA-InTec-0630, AEA Technology (2008)
54. N.M. Larson, Updated users' guide for SAMMY: Multilevel R-matrix fits to neutron data using Bayes' equations. Tech. Rep. ORNL/TM-9179/R8, Oak Ridge National Laboratory (2008). URL https://info.ornl.gov/sites/publications/files/Pub13056.pdf
55. H. Derrien, et al., Neutron resonance parameters of 238u and the calculated cross sections from the reich-moore analysis of experimental data in the neutron energy range from 0 kev to 20 kev. Tech. Rep. ORNL/TM-2005/241, Oak Ridge National Laboratory (2005)
56. R.L. Macklin, J.H. Gibbons, Neutron capture data at stellar temperatures, Rev. Mod. Phys. **37**, 166 (1965). DOI 10.1103/RevModPhys.37.166
57. H. Beer, F. Voss, R.R. Winters, On the calculation of maxwellian-averaged capture cross-sections, Astrophys. J. Suppl. Ser. **80**(1), 403 (1992). DOI 10.1086/191669
58. A. Mengoni, T. Otsuka, M. Ishihara, Direct radiative capture of p-wave neutrons, Phys. Rev. C **52**, R2334 (1995). DOI 10.1103/PhysRevC.52.R2334
59. S. Cristrallo, et al., Evolution, Nucleosynthesis, and Yields of Low-Mass Asymptotic Giant Branch Stars at Different Metallicities **696**, 797 (2009). DOI 10.1088/0004-637X/696/1/797
60. D. Vescovi, S. Cristrallo, M. Busso, N. Liu, Magnetic-buoyancy-induced Mixing in AGB Stars: Presolar SiC Grains **897**, 25 (2020). DOI 10.3847/2041-8213/ab9fa1
61. D. Vescovi, S. Cristrallo, S. Palmierini, C. Abia, M. Busso, Magnetic-buoyancy-induced mixing in AGB stars: Fluorine nucleosynthesis at different metallicities
62. S. Cristrallo, et al., The Importance of the 13C(,n)16O Reaction in Asymptotic Giant Branch Stars **859**, 105 (2018). DOI 10.3847/1538-4357/aac177
63. S. Cristrallo, et al., Evolution, Nucleosynthesis, and Yields of Low-mass Asymptotic Giant Branch Stars at Different Metallicities. II. The FRUITY Database

Table 4 Resonance parameters derived from a fit to the GELINA data. The quoted uncertainties are only due to propagating counting statistics uncertainties.

E_R (eV)	ℓ	J	Γ_γ (meV)	Γ_n (eV)	K (meV)	$g\Gamma_n$ (eV)
2597.39(2)	0	1	97(4)	0.790(9)	64.7(2)	0.593(7)
2608.02(1)	1	1	473(16)	1.56(1)	272(7)	1.17(1)
3381.37(1)	1				52.5(2)	0.274(6)
4778.3(1)	1	2	821(360)	0.022(1)	26.5(14)	0.027(1)
5714.3(1)					93(3)	0.199(1)
7501.9(2)	0	0	72(2)	58.8(4)	18.1(4)	14.7(1)
9418.1(1)	1				116(4)	2.70(1)
9735.99(1)	0				80(1)	0.8(1)
10732.2(3)					19.0(15)	0.17(2)
11583.8(2)	0	0	126(1)	83(1)	31.5(2)	20.8(1)
11586.63(1)	1				161(2)	6.71(1)
13007.2(1)	1				213(2)	7.01(2)
13804.7(3)	0				71(3)	1.03(9)
14075.6(2)					6.4(9)	0.007(1)
14225.73(4)					93(3)	2.03(6)
14535.70(2)					83(6)	0.187(2)
15209.6(1)	0	0	206(19)	58(3)	51(5)	14.6(6)
15216.9(1)	1	1	16(4)	9.0(4)	12(3)	6.7(3)
16591(1)					9.3(12)	
17120.1(9)					23(3)	
18587(2)					13(2)	
20302.2(2)	1				149(4)	3.3(2)
22125(1)					38(8)	
23036.85(3)	1	2	236(3)	25.8(4)	292(4)	32.2(6)
23665(2)					27(3)	1.2(2)
24097(2)					4(2)	2.8(4)
24141(2)					30(5)	3.3(7)
24174.9(1)	1				80(7)	11(1)
24579(2)	1				17(5)	4.2(5)
24619.5(5)	1	2	242(8)	33.1(6)	300(10)	41.3(7)
26427(2)					22(1)	13.8(3)
26779(4)					11(1)	0.9(2)
26901(1)					64(3)	3.1(3)
28175.8(7)	1				264(8)	5.8(4)
29316.3(6)	1	2	200(2)	60.4(8)	250(3)	76(1)
29577(1)	0	1	163(5)	89(1)	122(4)	66(1)
30123(1)	1	1	276(5)	41.0(9)	205(4)	30.8(7)
32905(1)					109(3)	12.1(6)
33479(2)					67(18)	
34811(1)	1	1	150(9)	91(2)	112(7)	68(1)
35469(7)					16(7)	2.1(9)
35501(5)					49(26)	10(1)
36893(4)					30(8)	
37082(6)					21(6)	
38030(2)					98(8)	8.2(9)
38278(2)	1				211(18)	17(2)
38323(2)					94(11)	5.5(8)
38864(5)					29(7)	
40975(2)					131(10)	12.2(9)
41497(5)					44(7)	
42091(2)	0	1	120(3)	84(2)	90(3)	63(2)
42342(8)					25(7)	
42687(3)					93(6)	2.4(8)
44361(4)					44(14)	
45707(5)					42(12)	
46071(3)					87(15)	
50243(2)					195(10)	3.3(2)
50593(5)					52(8)	
51662(2)	1	2	279(16)	39(1)	347(19)	49(2)
52072(2)					88(13)	32(2)
52136(5)					79(14)	9(2)
52895(13)	0	0	141(83)	867(35)	35(20)	217(9)
53828(3)	0	1	264(25)	30(2)	196(19)	22(2)
55295(3)	1				233(6)	33(2)
56061(4)	0	1	81(3)	49(4)	61(2)	37(3)
56286(4)	1				178(7)	54(3)
56363(7)					80(7)	16(3)
56540(3)	1	2	179(9)	5(2)	217(11)	7(2)
58984(4)					84(14)	
61098(4)					116(30)	
61653(3)					205(16)	13(2)
62429(6)	1	1	359(19)	166(12)	268(13)	125(9)
62629(3)	1	2	118(6)	116(6)	147(7)	146(7)
63016(9)					65(13)	2.8(17)
64617(4)	0	1	206(6)	44(3)	154(5)	33(2)
65410(4)	1				116(13)	63(3)
65894(8)					73(14)	
67585(2)					30(9)	2.3(14)
67746(4)	0	1	96(23)	117(5)	72(17)	87(4)
68559(3)	1				190(2)	167(4)
69009(14)					32(13)	
69749(6)					102(5)	12.6(2)
70477(1)	1	1	457(10)	105(5)	341(7)	79(4)
71443(20)					28(12)	
72043(8)					82(27)	
74434(6)					153(10)	7(2)
74628(9)					64(28)	
75042(4)					202(19)	12(3)
75248(18)					10(3)	10(3)
75679(7)	1				228(28)	137(8)
75908(8)					190(18)	12(5)
76161(6)					107(8)	98(5)
76631(8)					36(2)	13(2)
76932(4)					267(27)	137(6)
77163(20)					73(30)	57(7)
77278(19)					42(22)	
78893(9)					123(35)	
79474(11)					85(19)	
82858(17)					47(21)	12(3)
83091(15)					83(42)	9.9(15)
83119(22)					173(64)	190(13)
83475(5)					228(27)	82(8)
84776(8)					42(16)	
85163(8)					174(33)	30(3)
85382(7)					542(48)	183(9)
87308(15)					68(25)	
89189(26)					52(17)	3.4(21)
89795(5)					345(9)	231(8)
91082(11)					131(11)	7(4)
91716(6)					254(12)	17(4)
92483(8)					238(8)	129(8)
94038(7)					264(25)	19(4)

Table 5 MACSs for kT from 5 to 100 keV. The contribution from the capture kernels of observed resonances plus a $1/v$-contribution is given in the second column. The contribution for energies above 95 keV is calculated from cross section data in the JENDL-5.0 library [23]. This contribution is given in the third column. The total MACSs derived from experimental data complemented with the contribution obtained from the JENDL-5.0 library is presented in the last column.

kT	kernels + $1/v$ $E_n < 95$ keV	JENDL-5.0 $E_n > 95$ keV	Total MACS full range
(keV)	(mb)	(mb)	(mb)
5	72.2(36)	$\approx 10^{-2}$	72.2(36)
8	49.5(21)	$\approx 10^{-2}$	49.5(21)
10	41.4(17)	0.1	41.5(17)
15	30.2(11)	0.2	30.4(11)
20	24.1(9)	0.6	24.7(9)
23	21.4(8)	1.0	22.4(8)
25	20.0(7)	1.3	21.3(8)
30	17.0(6)	2.1	19.1(7)
35	14.7(5)	2.9	17.6(6)
40	12.8(5)	3.6	16.4(6)
45	11.3(4)	4.3	15.6(6)
50	10.0(4)	4.9	14.9(6)
55	9.0(3)	5.4	14.4(5)
60	8.1(3)	5.8	13.9(5)
70	6.7(2)	6.5	13.2(5)
80	5.6(2)	7.0	12.6(5)
90	4.8(2)	7.3	12.1(5)
100	4.1(1)	7.5	11.6(4)